Development and application of a computational fluid dynamics methodology to predict fuel–air mixing and sources of soot formation in gasoline direct injection engines

Tommaso Lucchini[1], Gianluca D' Errico[1], Angelo Onorati[1], Giovanni Bonandrini[2], Luca Venturoli[2] and Rita Di Gioia[2]

Date received: 12 March 2013; accepted: 12 July 2013

Introduction

Direct injection technology applied to spark-ignition (SI) engines ensures advantages in terms of improved thermal efficiency, better engine response during load variations, reduced knock tendency and lower pollutant emissions during cold start and transient modes. The possibility to operate under the stratified-charge mode reduces also the pumping losses at partial load, since the engine power output can be regulated only by variation of the injected fuel mass.[1] However, due to the current generation of after-treatment devices based on three-way catalysts, only homogeneous operation is allowed in most of the engine operating map with fuel delivered during intake and compression strokes through a multihole, mini-sac injector with pressures ranging from 1 to 20 MPa.[2] To enhance mixing between air and fuel and reduce wall-wetting, a proper design of the combustion chamber and spray patterns is necessary, including the possibility to increase organized charge motions (swirl/tumble) through partial intake port deactivation at low loads. Nevertheless, the limited amount of time that is generally available for the fuel to evaporate and mix with air is responsible for unavoidable charge inhomogeneities and liquid impingement of the cylinder walls. In particular, excessive wall-wetting or imperfect mixing produce hydrocarbon (HC) and soot that should be controlled mainly at

[1]Department of Energy, Politecnico di Milano, Milano, Italy
[2]Magneti Marelli Powertrain, Bologna, Italy

Corresponding author:
Tommaso Lucchini, Department of Energy, Politecnico di Milano, Via Lambruschini, 4, Milano 20156, Italy.
Email: tommaso.lucchini@polimi.it

high-load conditions, when the amount of fuel to inject is high.[3,4] Within this context, experimental and modeling efforts were focused toward the understanding of the relevant engine parameters governing the fuel–air mixing process and affecting soot formation. Injection pressure, strategy and wall-film dynamics were found to be the most important ones.[5–7] In particular, the use of high pressures (up to 1000 bar) or multiple injections can reduce particulate emissions and, at the same time, extend the engine operation under stratified-charge mode. This is mainly due to the higher atomization of the liquid jet, producing smaller droplets with fast evaporation and higher diffusion in the ambient air. Both these aspects compensate the corresponding increase in spray penetration. Investigation of fuel–air mixing and combustion processes involves many complex physical phenomena related to evolution of turbulent, multiphase flows, and for this reason, both advanced experimental optical techniques and multidimensional numerical models are necessary. Despite the fact that optical engines can properly reproduce modern gasoline direct injection (GDI) combustion chambers,[8,9] only a reduced set of geometry configurations and operating conditions can be analyzed, due to the high maintenance costs and problems related to thermal evolution, blow-by and capability to guarantee a satisfactory optical access also in presence of complex piston bowl shapes. Hence, the use of computational fluid dynamics (CFD) can represent an alternative solution, making it possible to test a significant variety of configurations in a limited amount of time.[10,11] However, simulation of fuel–air mixing in GDI engines involves many interacting phenomena that should be taken into account and still represents a very challenging task for CFD modeling. The complete evolution of the fuel spray, including the liquid film dynamics, should be described. Furthermore, reliable mesh management algorithms are necessary to preserve the grid quality in presence of moving boundaries of complex shapes like piston bowl, cylinder head and valves.

This work is focused on the development of a CFD methodology that can be applied to study the effects of fuel–air mixing on soot formation in GDI engines. A complete set of models was implemented to properly describe the evolution of liquid sprays emerging from multihole atomizers and interacting with cylinder walls. A simplified one-dimensional (1D) model of the nozzle flow was used to properly initialize the liquid jet diameter, velocity and angle. The Huh–Gosman model was used to predict the liquid jet atomization that was assumed to be affected by both turbulent and aerodynamic instabilities on its surface. Operation of the Huh–Gosman model includes both liquid jet diameter reduction and formation of secondary droplets whose diameter is sampled from a probability density function (pdf) distribution that is related to the size of turbulent eddies existing on the jet surface.[12] For what concerns the secondary droplets, both Kelvin–Helmholtz and Rayleigh–Taylor breakup mechanisms were considered to be the most relevant ones.[13] Despite the fact that both the approaches that proposed to simulate primary and secondary breakup were extensively consolidated over the years with simulation of diesel sprays, they were never applied to GDI engine cases, where the size of the droplets that are introduced in the computational domain is usually sampled from experimental Sauter mean diameter (SMD) data and all the breakup mechanisms are neglected.[14,15] However, such strong assumption has very limited predictive capabilities, affecting negatively both momentum exchange and evaporation in the near-nozzle region. The use of suitable models for both primary and secondary breakup is expected to significantly improve the predictive capabilities of the proposed approach, ensuring reasonable results in a wide range of operating conditions, including variation of injection pressure, injection timing (homogeneous or stratified), engine speeds and load.

Different impinging regimes were also considered: adhesion, rebound and splash with suitable correlations to compute size and droplet velocity after impact with walls.[16] The complete dynamics of the liquid film was also described in detail, including all the phenomena that are relevant for the fuel–air mixing process, such as droplet impact, shear induced by the gas flow, heat transfer, film evaporation and secondary atomization at sharp corners. Equations of film mass, momentum and energy conservation are solved on the mesh boundary by using the finite-area method. Effects of surface curvature are also taken into account. The Reynolds-averaged Navier–Stokes (RANS) approach was used for turbulence, because of its reliability and reduced central processing unit (CPU) time that it ensures compared to the more sophisticated discrete-event simulation (DES) or large-eddy simulation (LES) models. The proposed CFD approach has been developed using the Lib-ICE code, based on the OpenFOAM technology[17] and extensively applied in past works to model in-cylinder flows, fuel–air mixing and combustion in engines.[18–20] The choice of using the OpenFOAM technology was mainly justified by its open-source and C++ object-oriented structure. Over the years, both these aspects allowed the authors to build a specific framework to model internal combustion (IC) engines, where different libraries were developed in isolation to handle mesh motion and describe fuel spray evolution. Specific solvers are then created from combination of different library components: in this way, interaction between different models is easily handled, and very complex physical processes can be simulated. The methodology described was then validated in two steps: first the complete spray model was assessed with experiments at constant-volume conditions for different injection pressures. Then, the gas-exchange and fuel–air mixing phases were simulated for a turbocharged, GDI engine. Two operating points at full load were selected, and the effects of two different injector configurations were evaluated. For each simulated condition, a detailed postprocessing was performed at

Table 1. Liquid fuel properties at injection temperature (360 K).

Density	636 kg/m^3
Dynamic viscosity	2.5×10^{-4} Pa s
Surface tension	0.013 N/m
Vapor pressure	0.7 bar

spark-timing in order to correlate experimental data of soot emissions with computed uniformity index, wall-film mass and air–fuel ratio distribution. The results of such investigation proved that the proposed approach can be successfully applied to understand how spray targeting and combustion chamber design influence soot formation in GDI engines.

Computational models

The following sections illustrate the computational models developed by the authors within the Lib-ICE code to simulate gas exchange and fuel–air mixing in gasoline, direct-injection engines. In particular, a detailed description of moving mesh algorithms, spray and liquid film models is provided. All the simulations were carried out using the RANS approach with the standard $k-\varepsilon$ model for turbulence. Gasoline was approximated to be a single-component fuel, with both liquid and vapor properties assumed to be the same of pure iso-octane. The gas phase was treated as mixture of perfect gases, and Janaf polynomials were used to compute its thermodynamic properties. National Institute of Standards and Technology (NIST) tables were used to estimate temperature dependency of the liquid properties of the fuel, such as surface tension, heat of evaporation, vapor pressure and density. Liquid fuel properties at injection temperature (360 K) are summarized in Table 1. Despite the fact that properties of gasoline and iso-octane are somewhat different, this approximation is the common practice for CFD simulations of direct injection engines,[15,14] and it produces reasonable results. For this reason, this assumption was retained also in this work.

Mesh management

The proposed approach for CFD simulation of IC engines is illustrated in Figure 1. A multiple number of meshes are employed, so that each mesh is valid in a certain crank angle interval, and the grid points are moved and its topology can be eventually changed. Both commercial and open-source tools can be used for mesh generation, whose total amount for a full-cycle simulation depends on complexity of the combustion chamber geometry and the eventual use of topological changes. An automatic mesh motion technique, based on the Laplace equation, was developed to accommodate the motion of internal grid points according to the prescribed boundary motion.[21,22] Polyhedral grids are supported, and this aspect is quite important when

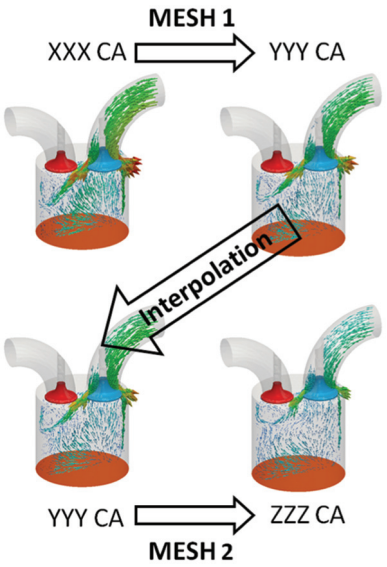

Figure 1. Summary of the strategy used for internal combustion engine simulation with moving meshes. Each mesh is used for a user-specified interval.

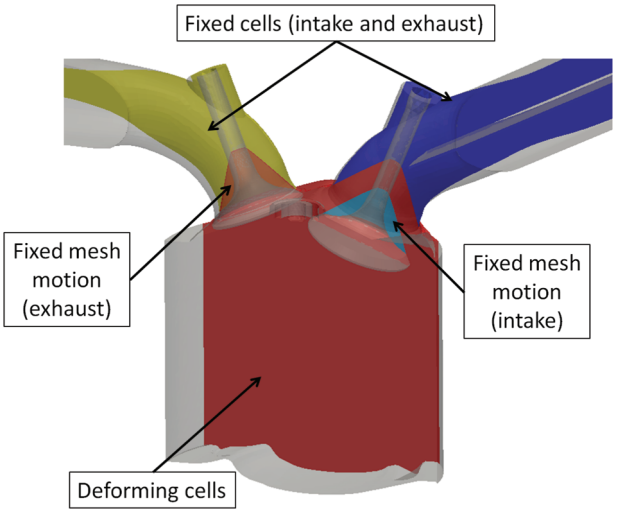

Figure 2. Mesh motion setup for GDI engine deforming grids.

GDI engines have to be simulated, since their complex geometry usually requires combination of hexahedrons and tetrahedrons in regions where high deformations take place. A typical layout to be used for GDI engine geometries is illustrated in Figure 2, where the following regions can be distinguished:

1. Fixed cells, in the intake and exhaust ports, together with zones in the cylinder where motion is not necessary (injector cavity, cells around the spark-plug);
2. Cells moving with valve velocity. They can be usually found over the poppet of the valve;
3. Deforming cells, whose displacement derives from solution of Laplace equation of motion.

Spray model

The spray is modeled using the Eulerian–Lagrangian approach and supports multicomponent fuels. Specific submodels are available to describe fuel atomization, breakup, heat transfer, evaporation, collision and wall impingement.

To properly predict the entire fuel spray evolution, attention needs to be focused on the two following physical phenomena:

- Generation of liquid droplets due to the interaction between the liquid jet and surrounding air, known as *atomization* or *primary breakup*;
- Diameter variation of secondary droplets is due to the instabilities taking place on its surface.

In this work, the atomization process is predicted by the Huh–Gosman model.[12] The liquid jet is represented by primary parcels (*blobs*) that are introduced within the computational mesh with the same nozzle diameter. Their velocity is function of the injected mass flow rate profile. Both Kelvin–Helmholtz and turbulence induced breakup on the jet surface are taken into account by the model, describing the diameter reduction of the injected parcels as follows

$$\frac{dD}{dt} = -C_5 \cdot \frac{L_a}{D_a} \tag{1}$$

where C_5 is the main model constant, L_a and D_a are the characteristic atomization length and time scales. L_a is proportional to the turbulent length scale on the liquid jet L_t, while atomization time-scale is function of both turbulent and aerodynamic time scales, τ_t and τ_w as follows

$$\tau_a = C_3 \cdot \tau_t + C_4 \cdot \tau_w \tag{2}$$

A zero-dimensional turbulence model was used to estimate the evolution of turbulent kinetic energy k and dissipation rate ε on the jet surface, that are initialized by a zero-dimensional nozzle flow model to accomplish the pressure losses inside it. From such quantities, values of L_t and τ_t can be directly computed. At the nozzle exit, the spray angle α is predicted according to the expression

$$tan\left(\frac{\alpha}{2}\right) = \frac{L_a/\tau_a}{U} \tag{3}$$

where U is the droplet velocity at the nozzle exit.

As a consequence of the parent droplet diameter evolutions, new droplets are created. The total stripped mass is calculated as

$$m_s = \rho_l \cdot n_p \cdot \frac{\pi}{6} \cdot \left(D_{old}^3 - D_n ew^3\right) \tag{4}$$

where n_p is the total number of parent droplets constituting the liquid core, D_{old} is the diameter of the droplet at the beginning of the time-step, while D_{new} is its value at the end, computed from equation (1). New parcels representing these stripped droplets are created when the total stripped mass is higher than a specific threshold, set to be equal to 0.05 times the original parent parcel mass, following Huh and Gosman.[12] The pdf for secondary droplet diameter is proportional to the turbulence energy spectrum and inversely proportional to atomization time-scale. Furthermore, it is based on the assumption that an eddy motion with larger kinetic energy and a shorter atomization time is likely to appear as an atomized droplet more frequently. The pdf is

$$p(x) = C\frac{\Phi(x)}{\tau_a} \tag{5}$$

where $\Phi(x)$ is the energy spectrum[23]

$$\Phi(x) = C\frac{(k/k_e)^2}{\left[1 + (k/k_e)^2\right]^{11/6}} \tag{6}$$

with the constant C that is determined by the normalization condition

$$\int_0^\infty p(x) = 1 \tag{7}$$

the wave number k is the inverse of the droplet diameter x and k_e is obtained from

$$k_e = \frac{1}{L_e} = \frac{1}{0.75L_t} \tag{8}$$

where L_e is the size of the eddies with the maximum energy in the turbulence energy spectrum.[23] The maximum diameter of the droplet size distribution is assumed to be the nozzle 1, while the minimum diameter is computed as

$$d_{min} = 2 \cdot \pi \frac{\left(\rho_{liq} + \rho_{gas}\right) \cdot \sigma}{\rho_{liq} \cdot \rho_{gas} \cdot U^2} \tag{9}$$

where σ is the liquid surface tension. The pdf distribution resulting from the previous assumptions mainly relates the size of the secondary droplets to the one of the eddies that are generated by turbulence on the jet surface, with computed diameters ranging between 0.01 and 0.2 times the original jet diameter. The Weber number of such droplets is still much higher than the stable value (~6), and hence, they undergo secondary breakup. Two different competing mechanisms were considered here: Kelvin–Helmholtz (*wave or KH*) and Rayleigh–Taylor (*catastrophic or RT*). In the first breakup mode, small child droplets with size D_{KH} are stripped from parent 1, whose diameter reduction is controlled by a breakup time τ_{KH} as follows

$$\frac{dD}{dt} = -\frac{D - D_{KH}}{\tau_{KH}} \tag{10}$$

Values of D_{KH} and τ_{KH} are function of the most unstable growth rate (Ω_{KH}) and wave number (Λ_{KH}).[13] A model constant, called B_1, is incorporated into τ_{KH} and needs to be adjusted to match experimental data. Here, only secondary droplet diameter reduction is considered: creation of new droplets due to secondary stripping is not taken into account to avoid the generation of an excessive number of parcels. Catastrophic breakup occurs when the droplet life-time becomes equal to τ_{RT}, that is function of fuel surface tension, relative velocity, droplet size and liquid and gas densities. When Rayleigh–Taylor breakup takes place, droplet size is reduced to

$$d_{RT} = 2\pi\sqrt{\frac{3\sigma}{a(\rho_l - \rho_g)}} \tag{11}$$

where a is computed as

$$a = \frac{3}{4} c_D \frac{\rho_g u_{rel}^2}{\rho_l d} \tag{12}$$

with c_D being the drag coefficient, u_{rel} being the relative gas velocity and ρ_l and ρ_g being the liquid and gas densities, respectively. The model tuning constant is C_{RT} and operates directly on τ_{RT}. Following Clerides,[24] the droplet Weber number is used as a criterion to switch from atomization to breakup model. The proposed model for primary and secondary spray breakup is able to produce a realistic multimode droplet diameter distribution, which is determined by jet turbulence in the near-nozzle region and competition between KH and RT mechanisms faraway. This aspect positively affects the prediction of the air–fuel mixing process. In particular, air entrainment is regulated by the primary breakup process, where both liquid jet and secondary stripped droplet exchange a high amount of momentum with the gas phase because of their high velocities and diameters that are found close to the nozzle. Far from the nozzle, secondary breakup will regulate the size of the droplet during evaporation providing a proper distribution of the fuel vapor within the combustion chamber. Neglecting breakup and introducing already stable droplets in the domain negatively affects both air entrainment and fuel evaporation. Since the stable size is much smaller than the jet diameter, the result of this will be both a high evaporation rate of the fuel close to the nozzle and a reduced entrainment of air due to the reduced droplet size. Hence, a thinner and very rich fuel region will be predicted.

The interaction between the spray and the liquid film is described with the approach originally proposed by Bai and Gosman.[16] Generally, the collision between a drop and a wet surface may result in three different regimes: adhesion, rebounding and splashing.[25] There are a number of parameters characterizing the impingement regimes such as incident drop velocity; incidence angle; liquid properties, such as viscosity, temperature and surface tension; wall properties, such as surface roughness and temperature; wall-film thickness and so on. Some of these parameters can be combined to yield dimensionless parameters. The two most important numbers are the Weber number

$$We = \frac{\rho_l v_n^2 d}{\sigma} \tag{13}$$

which represents the ratio of the droplet's kinetic energy (v_n: velocity component normal to the surface, ρ_l: liquid density and d: droplet diameter) and its surface energy, and the Laplace number

$$La = \frac{\rho_l \sigma d}{\mu_l^2} \tag{14}$$

which measures the relative importance of surface tension and viscous forces acting on the liquid (μ_l: dynamic viscosity of liquid). For a dry wall, the transition criterion between adhesion and splash is given as[16]

$$Adhesion \Rightarrow Splash \quad We_{crit} = A \cdot La^{-0.18} \tag{15}$$

where the coefficient A depends on the surface roughness ($A = 2634$ in this work). In the case of an already wetted wall, the transition Weber numbers are

$$Rebound \Rightarrow Spread \quad We_{crit} \approx 5.0 \tag{16}$$

$$Spread \Rightarrow Splash \quad We_{crit} \approx 1320 \cdot La^{-0.18} \tag{17}$$

In the adhesion regime, the incoming droplets are assumed to coalesce to form a local liquid film. In the rebound regime, the droplet bounces off the wall and does not break up, but loses a small part of its kinetic energy by deforming the liquid film. A relationship developed for a solid particle bouncing on a solid wall[26] was used to determine the rebound velocity components. In the splash regime, expressions are provided for the ratio of splashed mass and total incoming mass (m_s/m_{in}), the sizes, velocities and ejection angles of the new droplets. For further details about the model, the reader is referred to Bai and Gosman.[16]

Heat transfer between the liquid phase and surrounding gas was modeled by using the Ranz–Marshall correlation, while droplet evaporation rate was computed from droplet size, Spalding and Nusselt numbers.[27] Following the CFD setup for spray simulations illustrated in Montanaro et al.,[20] effects of turbulent dispersion were not considered in this work, since this submodel does not provide any significant improvement to the computed spray morphology. Collision between droplets was also neglected. This last choice was mainly motivated by the significant computational overheads that a collision model introduces when multiple sprays have to be simulated in a complete engine geometry. Furthermore, droplet collision and coalescence are not expected to play a very important role for the simulated engine, since it runs only under the homogeneous mode, and most of the fuel–air mixing and evaporation processes take place far from the nozzle where the spray is very dispersed in the gas flow.

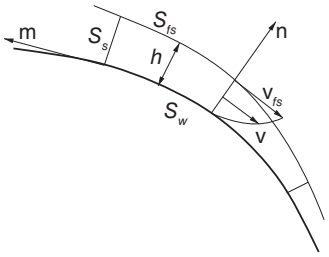

Figure 3. Schematic representation of a thin liquid film.

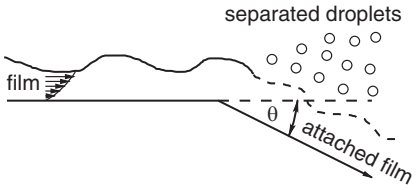

Figure 4. Film separation at a sharp corner.

Liquid film model

Figure 3 illustrates the schematic representation of a thin liquid film on a curved wall surface S_w, having normal **n**. The film has a variable thickness h and assumed velocity profile **v**, varying from zero at the wall to the free surface velocity $\mathbf{v}_{fs}$. The following assumptions were used to derive the governing equations for the liquid film:

- The film is thin enough for the boundary-layer approximation to apply, that is, the spatial gradients of the dependent variables tangential to the surface are negligible compared to those in the normal direction;
- Film motion is caused by spatial variation in the tangential directions in the total pressure p_L, shear at the wall and film interface, tangential momentum sources provided by incoming droplets and body forces (e.g. gravity acceleration);
- Under boundary-layer approximations, local liquid pressure p_L within the film can be taken to be constant across the film depth;
- Liquid pressure p_L consists of the following components: pressure of the surrounding gas p_g, droplet impact pressure p_d, capillary (or Laplace) pressure p_σ and hydrostatic pressure p_h. Thus, the liquid film is locally subject to the following pressure

$$p_L = p_g + p_d + p_\sigma + p_h \tag{18}$$

- The tangential momentum lost by the incident droplets provides a source of tangential momentum to the wall film;
- The mass flux due to incident droplets may be represented by a spatially smoothly varying function, so that conventional differential operations apply.

Governing equations for liquid film mass, momentum and energy includes effects of spray impingement and film evaporation.[16,28] At each time-step, the amount of evaporated film mass and corresponding energy is transferred to the gas phase. Mass, momentum and energy equations are solved using the segregated solution procedure, where the three equations are separately solved, and coupling is recovered through the iterative procedure. The liquid film equations were discretized on a curved two-dimensional (2-D) surface in three-dimensional (3-D), accounting for its curvature and motion using the Finite Area Method. Faces of arbitrary shapes are supported, therefore flexibility with respect to the mesh structure is ensured and complex geometries, like IC engines, can be simulated without any limitation.[18]

Fuel film separation

Depending on the injector configuration and strategy, fuel impingement can take place not only on the piston and cylinder surfaces but also on the valves where gas velocities are very high. As a consequence, the film is convected at the valve sharp edges, and when flowing around a corner, it can either stay attached or separate forming new droplets as illustrated in Figure 4.

Due to inertia, the film tends to keep its initial direction; for this reason, when it reaches a corner, a low pressure region is established at the wall-side of the film. The pressure difference between the wall-side and the gas-side causes the film to stay attached on the wall. Film separation is assumed to happen when the liquid inertia is so large that the wall-side pressure drops to zero. If the liquid inertia is so large that the wall-side pressure drops to zero, the film is believed to separate. In this work, the separation criterion proposed by O'Rourke was used.[29] Droplets are stripped from the liquid film when the following condition is fulfilled

$$c_{Sep}\frac{(\rho_F \cdot u_F)^2 \cdot sin(\theta)}{1 + cos(\theta)} > p_G \tag{19}$$

where c_{Sep} is a model constant set to 3.0, u_F is the magnitude of the liquid film velocity, ρ_F is the liquid film density, p_G is the gas pressure and θ is the angle between the two boundary faces, shown in Figure 4. The diameter of the new droplets created by film separation is assumed to be proportional to the film height

$$d_{d,\,stripped} = c_{diam} \cdot h \tag{20}$$

where c_{diam} is set to 1.9.

The proposed set of spray submodels and governing equations for the liquid film evolution makes it possible to account for all the mutual interactions between the gas, spray and liquid film phases. This aspect is very important for GDI engine simulations since the

Table 2. Main engine geometry data.

Displaced volume	1390 cm^3
Bore × Stroke	76.5 × 75.6 mm^2
Compression ratio	10:1
Valves per cylinder	4

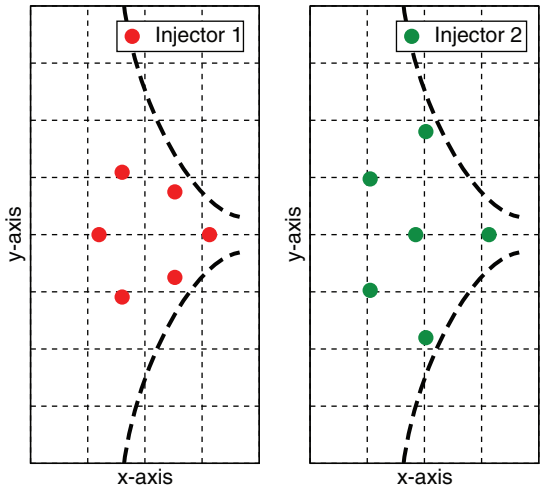

Figure 5. Spray patterns for (a) injector 1 and (b) injector 2 projected on a plane located 30 mm below the injector position. Dashed line: projected valve profiles at maximum lift.

fuel–air mixing process is determined by combination of in-cylinder flows, spray evolution and liquid film dynamics.

Validation of the CFD methodology

Engine details and selected operating conditions

Simulations of gas exchange and fuel–air mixing were carried out for a turbocharged, downsized, stoichiometric and side-mounted GDI engine whose main data are reported in Table 2.

The engine has variable valve timing on the intake side, and a tumble flap that can be used to enhance air–fuel mixing under certain operating conditions. Experimental tests were performed at steady-state conditions with two different fast-solenoid Magneti Marelli six-hole injectors, having very similar flow numbers, the same diameter and average length-to-diameter ratio ($d = 145\mu m$; $L/D = 1.5$). Figure 5 illustrates a schematic of the emerging spray patterns, projected on a plane located 30 mm below the injector position. In the same picture, profiles of the two intake valves at maximum lift are also reported to understand their possible interactions with fuel jets. Injector 1 is characterized by a relatively close spray pattern, while injector 2 shows a wider pattern with more distinct jets, reducing their interaction.

Experimental data of engine performance, in-cylinder pressure profiles and pollutant emissions (HC, CO and NO_x) were acquired. Furthermore, an AVL Particle Counter (APC) 489 was employed to measure soot particle concentration in the Condensation Particle Counter (PNC), with a size range of 23 nm to 2.5 μm according to UNECE-R83 specifications.

Table 3. Details of the simulated operating conditions.

	Engine point 1	Engine point 2
Speed (r/min)	1500	5500
BMEP (bar)	14.5	16.5
Spark advance (°ATDC)	5	−20
Start of injection (°TDC)	−275	−325
Energizing time (μs)	6000	3930
Injection pressure (bar)	80	130
Relative air/fuel ratio λ	1.0	0.9
Tumble flap	Off	Off

BMEP: brake mean effective pressure; TDC: top dead center; ATDC: after top dead center.

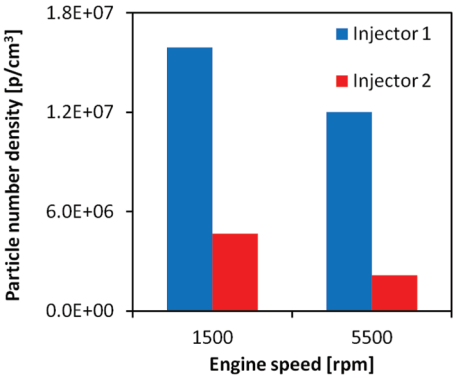

Figure 6. Soot production (particle number) for the selected operating points.

Two different operating points, at medium–high load conditions, were simulated with the tumble flap deactivated. Table 3 summarizes the main operating conditions in terms of speed, load and injection parameters. Both these points represent critical conditions for what concerns soot production during combustion process. Since a high amount of fuel is provided, injection system and strategy should be designed to minimize wall impingement and optimize the fuel distribution within the combustion chamber.

Figure 6 reports the particulate emissions for both the engine operating points and injector configurations. Despite the fact that no significant differences were found in terms of combustion efficiency, more soot is produced at 1500 r/min, and the amount of particles generated by injector 1 is significantly higher compared to those of the injector 2. The same trend was also found for CO and HC emissions, whose values are reported in Table 4. To better understand these differences, CFD calculations will be used as a diagnostic tool. In particular, a detailed postprocessing of the fuel–air mixing process was performed.

Table 4. Experimental CO and HC emissions for the simulated operating points.

	CO (%)	HC (ppm)
Injector 1—1500 r/min	0.65	616
Injector 1—5500 r/min	3.88	1516
Injector 2—1500 r/min	0.47	170
Injector 2—5500 r/min	2.79	1167

HC: hydrocarbon.

Table 5. Model constants used for spray simulations.

C_5	B_1	c_{RT}
2.0	6.0	0.05

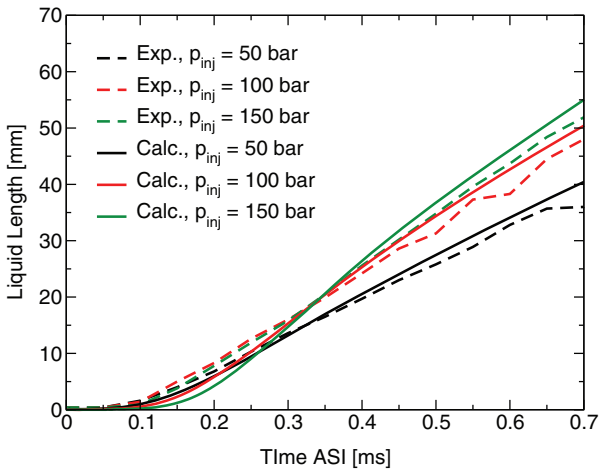

Figure 7. Comparison between computed and experimental data of spray penetration at constant-volume conditions for different injection pressures: 50, 100 and 150 bar.

Assessment and validation of the spray model

Experiments at nonevaporating, constant-volume conditions, performed with the same injector mounted on the engine were used to tune the proposed spray model. Fuel is injected in a cylindrical vessel, filled with nitrogen at 1 bar ambient pressure. A charge-coupled device (CCD) camera acquires the spray images that are then digitally postprocessed to measure the spray penetration. The well-known Phase Doppler Anemometry (PDA) optical technique was also employed to estimate the spray mean diameter at a 2 cm distance from the injector.

Profiles of injected mass flow rate were provided by simulations of the complete injection system performed with the AMESIM®code. The validity of the model was extensively verified by comparing computed and experimental data of injected mass for different energizing times.

The computational grid used for spray simulations reproduces part of the experimental vessel; approximately 100,000 cells were employed with a size of 1 mm in the spray region. Only the spray emerging from a single hole was modeled. Tuning of the spray model constants C_5, B_1 and c_{RT} was carried out by simulating an injection event with 100 bar pressure, where a total amount of 11 mg of fuel was delivered. In particular, the best matching in terms of spray penetration was found for the set of parameters shown in Table 5.

Using the same model constants, simulations were carried out at different pressures (50 and 150 bar), and computed results in terms of spray penetration are displayed in Figure 7. A rather good agreement between computed and experimental data was achieved in the second part of the injection phase, while predicted penetration is underestimated in the first part of the injection process until 0.2 ms. During this first phase, nozzle needle is moving, and internal nozzle flow might be affected by cavitation, with a consequent increase of the droplet velocity and cone angle reduction. Such effects are not taken into account by the proposed injection model, and this explains the discrepancy between computed and experimental data. During the steady-state part of the injection process, the model correctly reproduces the experimental dependency of spray penetration on the injection pressure.

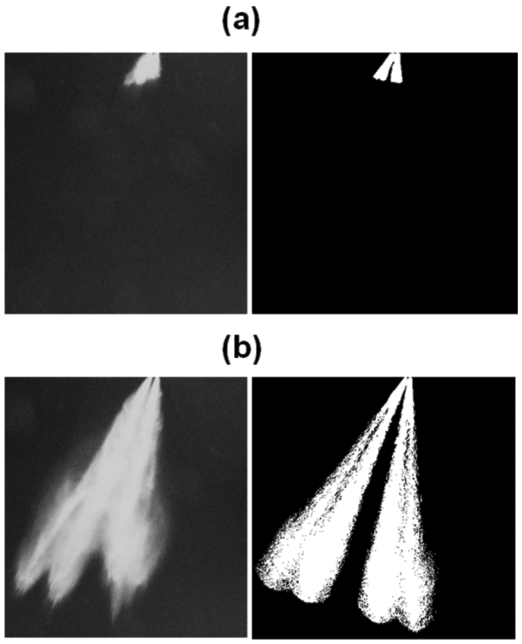

Figure 8. Comparison between experimental (left) and computed (right) evolution of the spray at 100 bar injection pressure at two different instants after start of injection: (a) t = 0.3 ms ASI and (b) t = 0.7 ms ASI.

To understand the discrepancies in the first part of the injection phase and evaluate the model capability to predict the spray morphology, Figure 8(a) and (b) reports a comparison between computed and experimental spray evolution at different instants after start of injection (SOI) for the 100 bar injection pressure

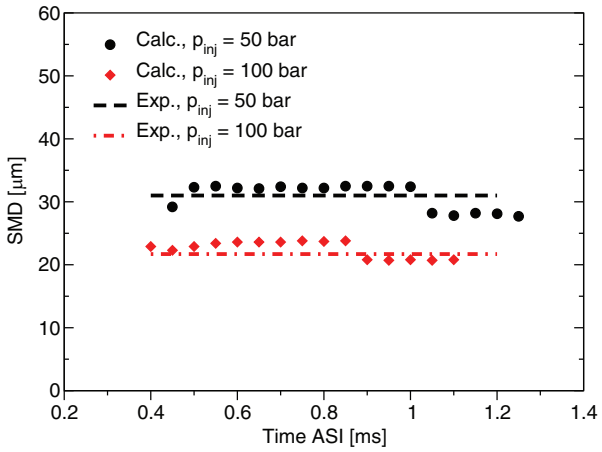

Figure 9. Comparison between computed and experimental data of SMD for the 50 and 100 bar injection pressure cases.
SMD: Sauter mean diameter.

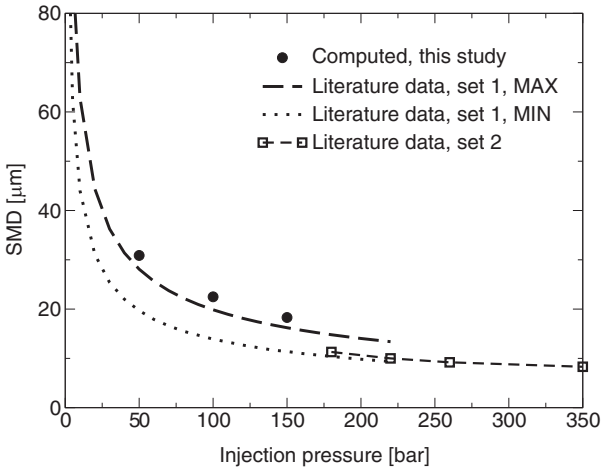

Figure 10. Comparison between computed data of SMD as function of injection pressure and experimental data suggested in set 1 and set 2.[30,31]
SMD: Sauter mean diameter.

conditions. All the six jets of the spray were taken into account, and Lagrangian particles were represented by squared points at their position. Initially, Figure 8(a) illustrates that one of the jets has a higher penetration, and this partially explains the discrepancy between computed and experimental data in the first part of the injection process. Afterwards, at 0.7 ms after the start of injection (SOI), the predicted spray shape is acceptable, and discrepancies are mainly due to the different way experimental and computed spray images were acquired.

A correct estimation of the droplet diameter is very important when sprays for GDI engines have to be simulated, since most of the fuel evaporates during intake and initial part of compression phases, when in-cylinder temperature remains almost constant (350 K $<$ T $<$ 450 K) and evaporation rate is mainly controlled by droplet size and relative velocity, following

$$\dot{m}_d = -\pi D D \rho_v Sh \ln\left(1 + \frac{Y_{v,s} - Y_{v,\infty}}{1 - Y_{v,s}}\right) \quad (21)$$

with D being droplet diameter, D being the mass diffusion coefficient, Sh being the Sherwood number and $Y_{v,s}$ and $Y_{v,\infty}$ being the fuel mass fractions at saturation conditions and in the gas phase, respectively.

Hence, Figure 9 compares computed and experimental values of SMD for the 50 and 100 bar injection pressure conditions. SMD experimental data were averaged in a 0–2 ms time interval, with sampling location placed 20 mm below the injector along the vessel vertical axis. The distance was chosen as close as possible to the injector tip, in order to properly evaluate the spray atomization and breakup processes. At such distance, it was verified that the PDA analysis allows to sample a sufficient number of droplets for a proper estimation of the SMD. A rather good agreement was achieved for both the conditions. For the sake of completeness and to further verify the proposed set of submodels, computed effects of injection pressure on SMD are compared with experimental data from Hammer et al.[30] and Sens et al.[31] in Figure 10. The trend in terms of droplet diameter reduction with increase of injection pressure is correctly reproduced.

Spray simulations provided satisfactory results both in terms of liquid penetration and droplet diameter. This aspect is very important since a proper validation of the spray model is a fundamental prerequisite for a successful simulation of the air–fuel mixing process in GDI engines.

Engine simulations

Mesh generation and case setup

The complete combustion chamber layout was discretized, including the intake and exhaust ports and accounting for the real shape of both the piston bowl and cylinder head. Since the geometry is fully symmetric, only half of it was meshed. Simulations start during the last part of the exhaust phase, 60° before top dead center (TDC), with uniform pressure and temperature fields set in the cylinder and exhaust duct. Unsteady pressure and temperature boundary conditions, taken from a 1D simulation of the whole engine system, were imposed at the inlet and outlet boundaries. Figure 11 displays the overall computational mesh: only hexahedral cells were adopted with a block-structured layout. The end of the simulation was set at spark-timing, and 24 meshes were used, with a validity interval of approximately 20° crank angle (CAD). The mesh resolution ranges from 150,000 to 600,000 cells.

To verify the validity of the proposed setup both in terms of mesh and boundary conditions, computed and experimental pressure profiles were compared in Figure 12(a) and (b) for both the simulated operating

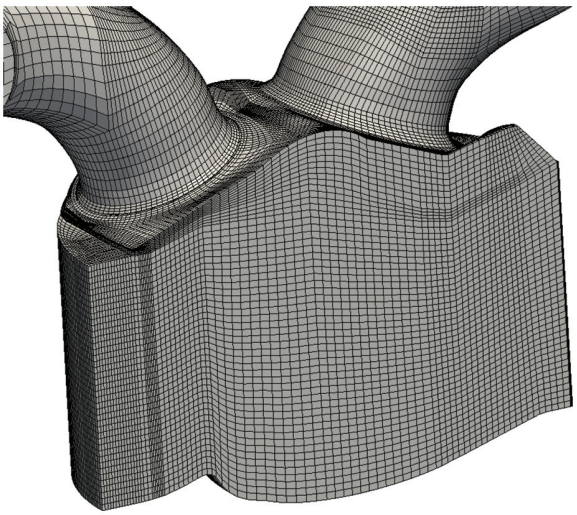

Figure 11. Computational mesh details of the simulated engine.

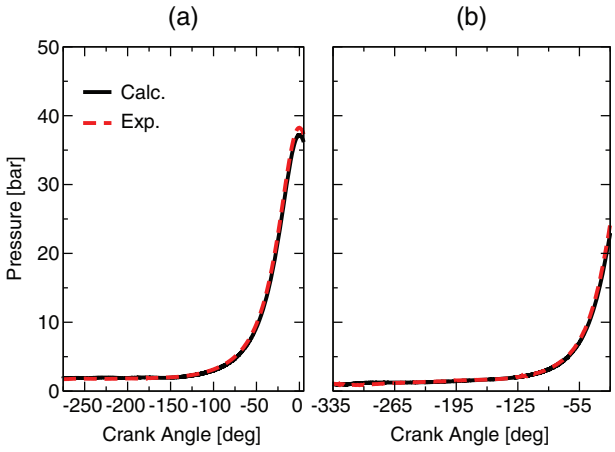

Figure 12. Comparison between computed and experimental in-cylinder pressure profiles for the two selected operating points: (a) 1500 r/min and (b) 5500 r/min.

conditions. A rather satisfactory agreement was achieved, and this ensures a correct estimation of the effects of in-cylinder pressure and temperature on fuel evaporation.

Details of the computed flow field at SOI time for the 1500 r/min condition are reported in Figure 13. On the left of Figure 13, velocity vectors are illustrated on the cylinder symmetry plane. On the right side, details of the incoming gas jet are shown. Despite the fact that the tumble flap was deactivated, it is possible to see that a weak tumble vortex is going to establish on the cylinder symmetry plane, which is induced by incoming air jet on the top right part of the intake valve. As a consequence of this, both spray targeting and in-cylinder flow field will determine the quality of the air–fuel mixture at spark-time.

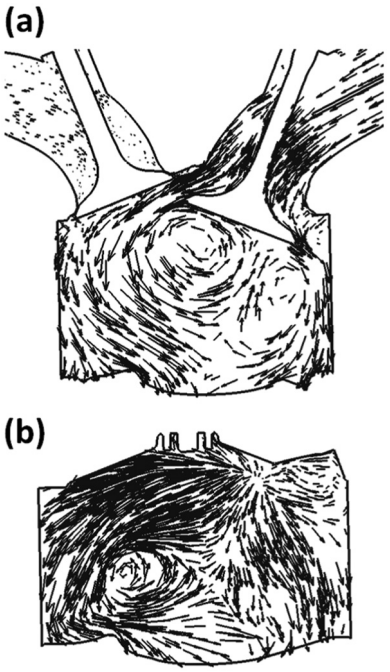

Figure 13. Computed in-cylinder flow field at start of injection time (275° before TDC) for operating point 1: (a) vertical plane passing through both the intake and exhaust valve axes and (b) cylinder symmetry plane. Maximum velocity = 30 m/s.

Fuel-air mixing simulations

Figure 14(a) and (b) illustrates evolution of fuel spray and liquid film at 1500 r/min for both the injector configurations. To understand how they differ in terms of jet morphology, interaction with the gas flow and liquid film formation, three different instants were displayed: 15° after SOI, end of injection and 630 CAD (half of compression stroke) when most of the fuel is expected to be in the vapor phase. Different colors were used in the pictures to identify the nozzle hole each droplet comes from. The deposited liquid film is displayed as well using dark green color. At 460 CAD, it is immediately possible to see that injector 2 has a wider opening angle which might have positive effects on droplet distribution inside the cylinder. For what concerns injector 1, interaction between one of its jets (the red one) and the intake valve is important and justifies the need to model formation of droplets from the liquid film.

When injection ends, at 500 CAD, droplets emerging from injector 1 are grouped along their patterns and in the region between piston crown and cylinder liner. The wider opening of the jets is responsible for a more homogeneous distribution of droplets inside the cylinder when injector 2 is used. Details of the impinged regions can be seen at 630 CAD, where it is possible to see that injector 1 produces a higher amount of wall film both on piston and cylinder liner. Figure 15 illustrates also how fuel impingement on the valve might affect the fuel–air mixing process: first liquid fuel is

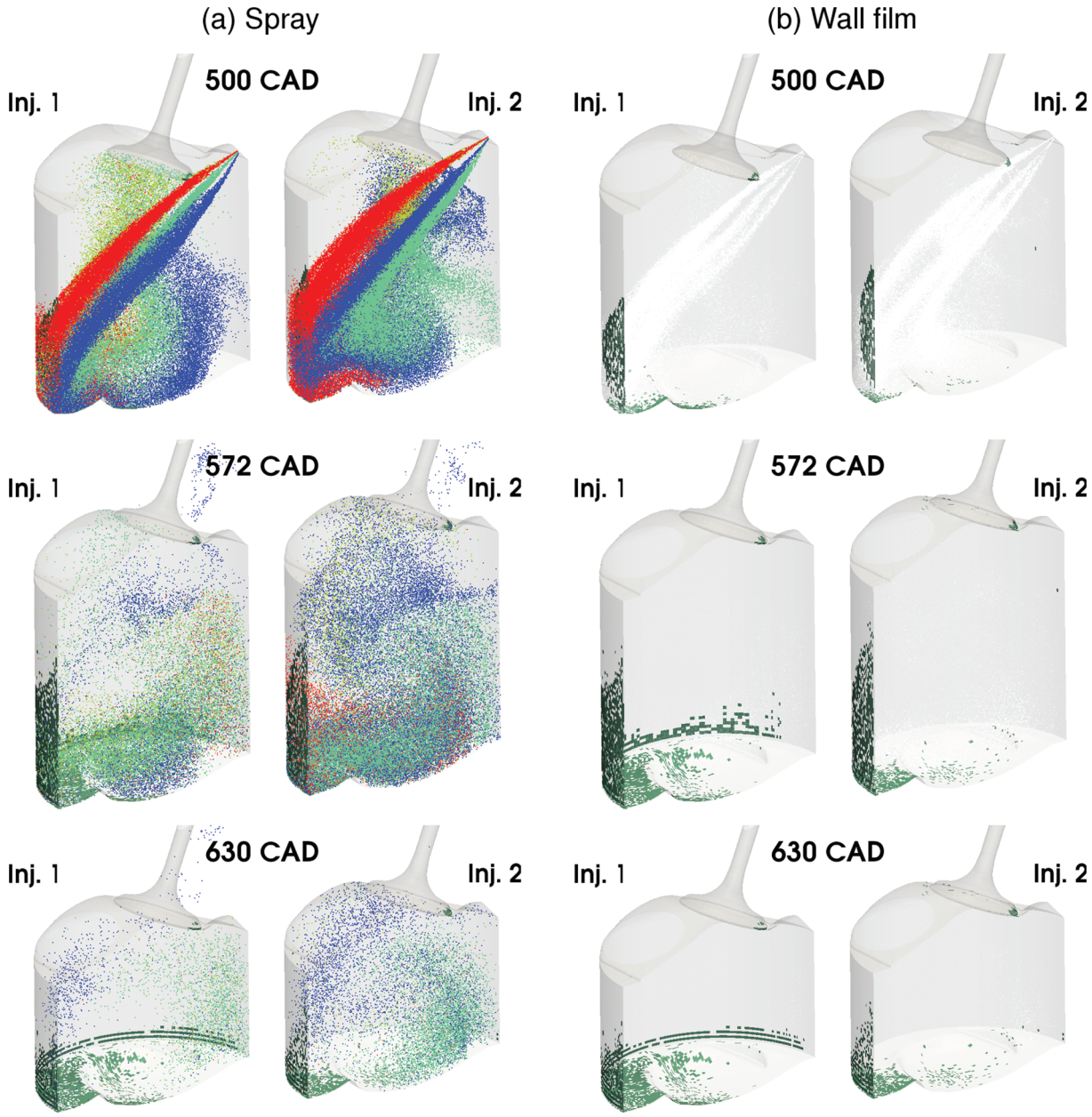

Figure 14. Operating point 1, 1500 r/min. Computed evolution of fuel spray and liquid film at different instants after start of injection: (a) Fuel spray distribution, different colors are used to distinguish the nozzle each parcel comes from and (b) liquid film formation and evolution. Liquid film colored with dark green.

deposited on the valve, and at the end of injection, the incoming air flow separates secondary droplets from the liquid film at the valve poppet edge. Trajectory and breakup of such new droplets is not related to spray targeting and injector properties, but it only depends on the air flow. Simulations illustrate that fuel film separation takes place when the film thickness on the edge of the valve is approximately 5 μm, and according to equation (20), the resulting diameter of stripped droplets will be close to 10 μm, which is smaller than the expected SMD for this spray (see Figure 9). However, in cases where significant spray impingement on the valves is going to take place, evolution of the separated droplets will be significantly different from the remainder of the spray, since their relative velocity is very small, and this results in reduced breakup and evaporation rates, with a consequent increase of charge inhomogeneities. For what concerns the simulated configurations, Figure 5 illustrates that only two jets have a limited interaction with the intake valves, and at intake valve closing (IVC) time, the computed amount of liquid film on the valve poppet surface is approximately 1% of what was found on the piston surface. These data suggest that fuel film separation has a very limited influence on the fuel–air mixing process for the considered spray patterns.

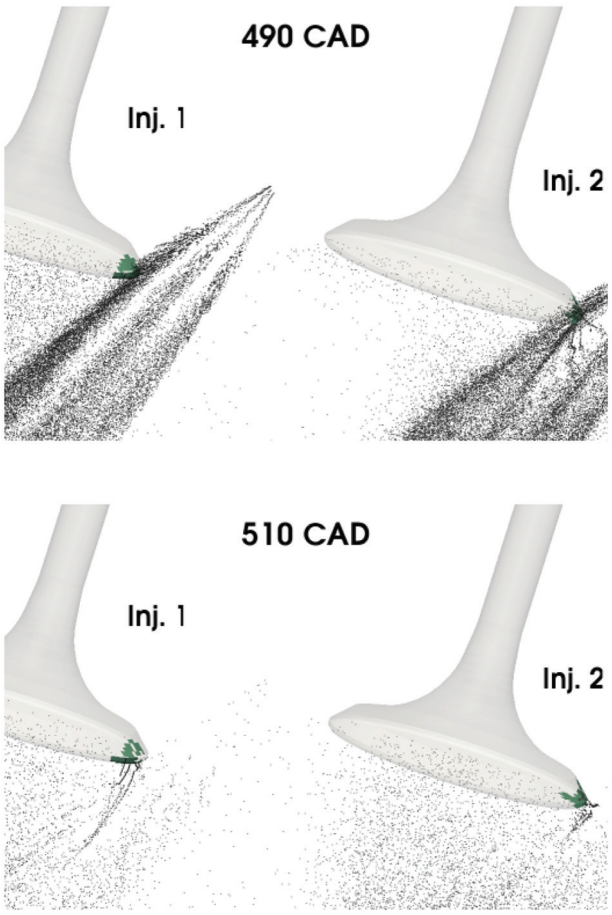

Figure 15. Liquid fuel deposition and film separation processes on the intake valve.

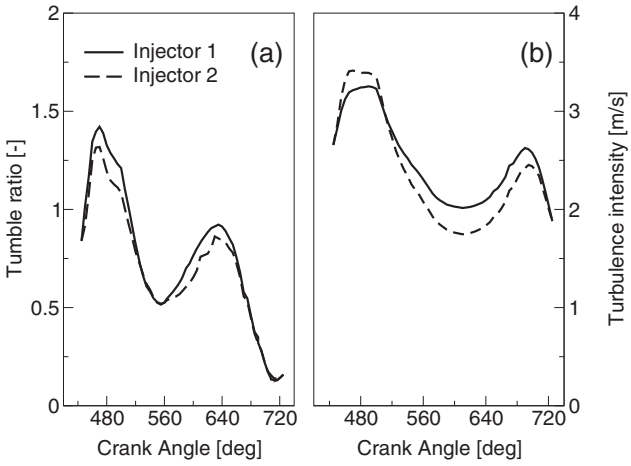

Figure 16. Effects of injector layout on (a) tumble ratio and intensity (b) in-cylinder turbulence.

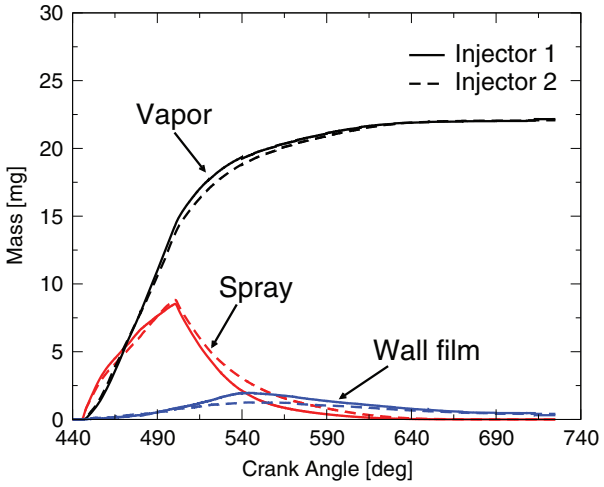

Figure 17. Effects of injector layout on computed evolution of fuel spray, vapor and liquid film mass for the operating point 1 (1500 r/min).

Such preliminary analysis already provides few hints about the higher particle emissions from injector 1. However, it is necessary to better quantify the contributions of the two different injectors in terms of in-cylinder turbulence, mixture inhomogeneity and deposited wall-film mass.

Effects of injection on charge motions evolution are summarized in Figure 16(a) and (b), where the computed profiles of tumble ratio and turbulence intensity are displayed for the 1500 r/min condition. When fuel is injected directly in the combustion chamber, tumble motion results from the complex interaction between the incoming gas jet and the flow generated by the spray momentum. For the entire fuel–air mixing process, tumble ratio remains well above the 0.5 value until half of the compression stroke. Then it decays rapidly when the piston approaches TDC, with a consequent increase of turbulent kinetic energy. At spark-timing, computed turbulence intensity is approximately half the mean piston speed, representing reasonable value due to the presence of a well-established tumble vortex. Both injector configurations produce very similar trends in terms of charge motions and in-cylinder turbulence, with minimal differences that can be ascribed to the different spray targeting layouts. Hence, it is possible to conclude that the main differences in terms of soot formation are mainly due to the air–fuel mixture distribution and deposited film mass, since none of the spray targets seem to promote combustion and in-cylinder mixing through enhanced turbulence.

Evolution of in-cylinder fuel vapor, spray and wall-film masses are displayed in Figure 17. A very similar behavior between the two injectors is found until 500 CAD: at that time two different processes, evaporation and liquid impingement reduce the spray mass in the cylinder. Liquid film formation is much more relevant for injector 1, whose reduction of free droplets is only partially compensated by evaporation. Once formed, liquid film evaporates slowly during compression. The total amount of liquid film is approximately 1.5% the injected fuel. Figure 18 provides few more details related to the liquid film mass evolution on both the liner and piston surfaces during compression stroke.

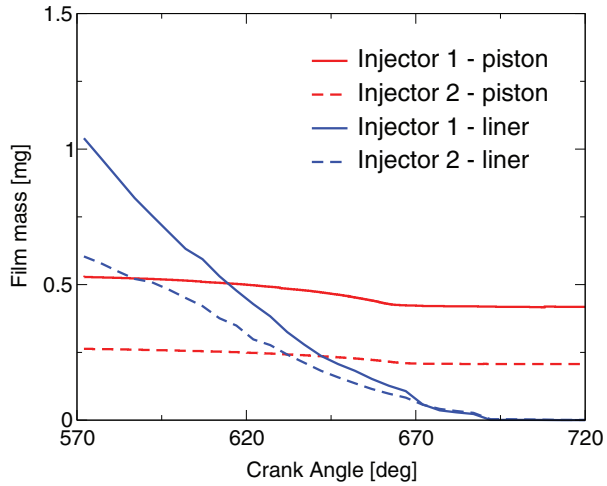

Figure 18. Effects of injector layout on computed evolution of liquid film mass on piston and cylinder liner surfaces during compression stroke for the operating point 1 (1500 r/min).

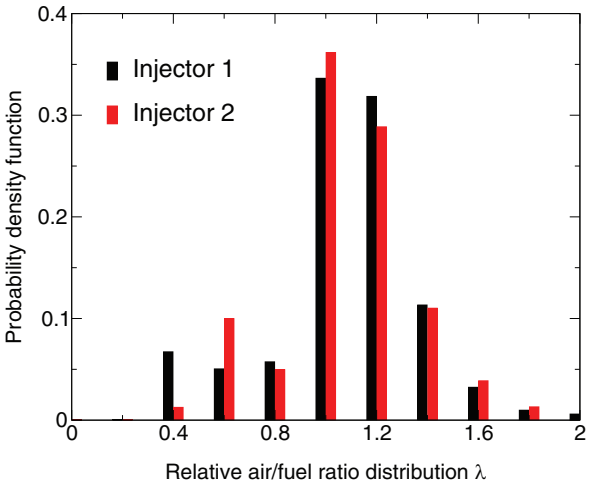

Figure 20. Effects of injector layout on computed distribution of the relative air/fuel ratio λ at spark-timing (5 CAD after TDC) for the operating point 1 (1500 r/min).

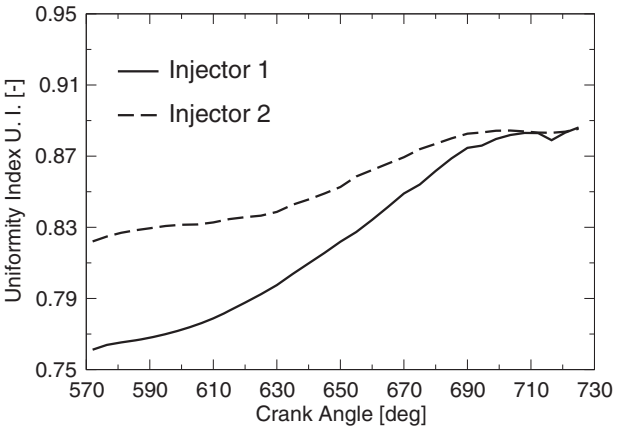

Figure 19. Effects of injector layout on computed evolution of in-cylinder homogeneity index during compression stroke for the operating point 1 (1500 r/min).

While the liquid mass in the cylinder liner completely disappears during compression, a non-negligible amount of fuel remains on the piston. In particular, injector 1 produces the highest amount of film mass, and this aspect is responsible for the formation of a higher amount of soot particles.

To understand contributions to soot emissions originated by charge inhomogeneities, the quality of the air–fuel mixing process is evaluated by looking at uniformity index evolution and distribution of air/fuel ratio. Uniformity index is a global quantity, defined as[32]

$$U.I. = 1 - \frac{\sigma}{\sigma_{n,h}} \tag{22}$$

where σ represents the standard deviation of the fuel mass fraction, while $\sigma_{n,h}$ is defined as the standard deviation in a completely inhomogeneous condition where the fuel is not mixed with air at all

$$\sigma_{n,h} = \sqrt{A/F} \Big/ (1 + A/F) \tag{23}$$

However, $U.I.$ is not completely representative of possible amount of fuel vapor in very rich zones and for this reason also the distribution of relative air–fuel ratio inside the cylinder has to be postprocessed. Evolution of uniformity index for injector 1 is illustrated in Figure 19 for the compression stroke. At the beginning of it, injector 2 presents a more homogeneous mixture due to better spray distribution and reduced wall impingement. However, uniformity differences are flattened during compression stroke due to film evaporation and tumble motion.

Finally, in-cylinder relative air–fuel ratio λ distribution is reported in Figure 20 at spark-timing, 5 CAD after TDC. As expected, most of the mixture is found in the 1.0–1.2 range for both the injectors since the engine is running with stoichiometric mixture. Despite the degree of charge homogeneity being very similar, it is possible to see that when injector 1 is mounted on the engine, a higher amount of fuel vapor exists in very rich zones ($0.3 < \lambda < 0.5$) that might lead to formation of soot.

The computational investigation carried out at 1500 r/min allowed to understand the two main sources of soot formation at this operating condition: fuel impingement on the piston and formation of rich zones inside the combustion chamber. Same phenomena are also responsible for higher CO and HC emissions when injector 1 was adopted.

The same investigation was also carried out at 5500 r/min, here only the most relevant differences with the previous analyzed condition are reported. Injection starts earlier due to increased speed, and interaction between the fuel jets and very high incoming gas velocities seems to be the most relevant process affecting air–fuel mixing.

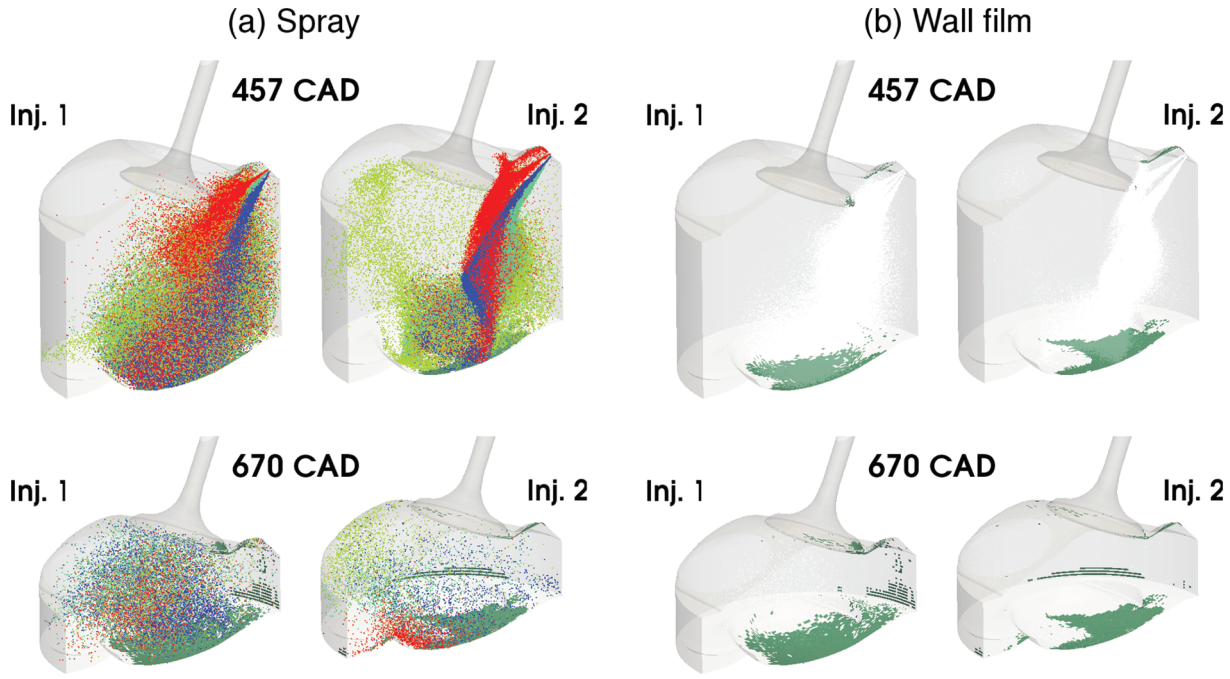

Figure 21. Operating point 2, 5500 r/min. Computed evolution of fuel spray and liquid film at different instants after start of injection: (a) fuel spray distribution—different colors are used to distinguish the nozzle each parcel comes from and (b) Liquid film formation and evolution. Liquid film colored with dark green.

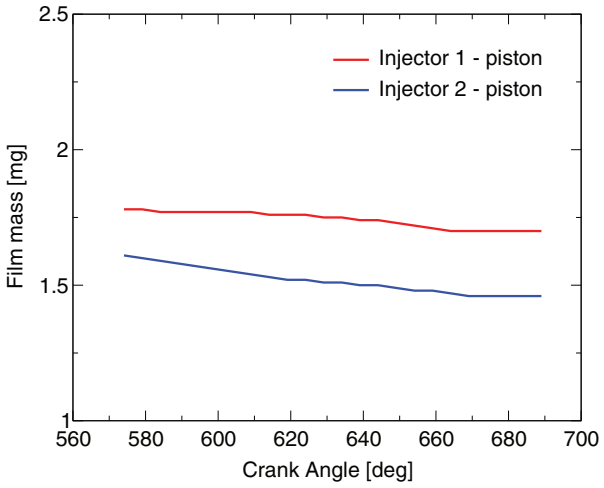

Figure 22. Effects of injector layout on computed evolution of liquid film mass on piston and cylinder liner surfaces during compression stroke for the operating point 2 (5500 r/min).

This can be clearly seen in Figure 21(a) and (b) at 457 CAD: fuel emerging from injector 2 is convected by the air flow directly towards the piston surface and most of the droplets remain confined between the piston and the intake valve. Injector 1 promotes the mixing between air and fuel, interacting with the air flow in a different way that better distributes the fuel inside the cylinder. In both the cases, impingement takes place only on the piston surface while a very small amount of fuel is deposited on the cylinder liner. A total of 30 CAD before spark, Figure 21 shows that for both injectors, there is still liquid fuel in the combustion chamber, but the impinged region is wider when injector 1 is used. This is confirmed by Figure 22, showing the evolution of liquid film mass on the piston during the compression stroke. The total mass of liquid on the piston at 5500 r/min is approximately three times the value at 1500 r/min. However, very similar particle emissions were found for both the engine speed. A possible explanation for this can be found in the highest amount of in-cylinder turbulence at 5500 r/min that might enhance after main combustion oxidation of soot particles with lean burned hot gases.

Relative air–fuel ratio distribution at spark-timing (20 CAD before TDC) is displayed in Figure 23. In this case, the way spray evolves and evaporates inside the combustion chamber determines significant differences between the two injector configurations. A very satisfactory distribution was found for injector 2 with most of the mixture located in the 0.8–1.2 λ range, while injector 1 produces a slightly stratified charge. However, since no fuel vapor was found in very rich zones for injector 1, the liquid film mass produced by such configuration is responsible for the higher amount of soot emissions.

Conclusion

This work focused on the development of a CFD methodology that can be used to identify possible sources of soot formation in GDI engines. A complete set of models was implemented into an open-source CFD code to

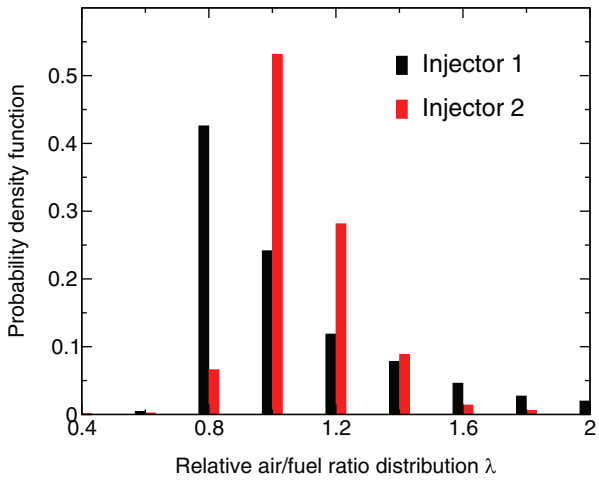

Figure 23. Effects of injector layout on computed distribution of the relative air/fuel ratio λ at spark-timing (20 CAD before TDC) for the operating point 2 (5500 r/min).

describe the evolution of both liquid spray emerging from multihole injectors and wall film. A detailed post-processing technique was used to properly characterize the quality of the mixture of air and fuel at spark-timing by analyzing the following data: evolution of in-cylinder charge motion intensity, turbulence, homogeneity index and amount of fuel found in spray, vapor and liquid film phases. For a successful application of the proposed CFD methodology, first the complete set of spray submodels was tuned to correctly predict liquid spray penetration and droplet diameter, since they both control fuel distribution and evaporation inside the combustion chamber. Then, the proposed spray setup was applied to simulate gas-exchange and fuel–air mixing processes in a turbocharged, GDI engine operating at two different speeds with two injector configurations. To properly identify possible sources of soot formation, computed distribution of equivalence ratio and deposited liquid film mass seems to be the most effective parameters that also correlate rather well with the experimental trend of particle emissions that was found for the tested. Results achieved are considered to be satisfactory, making it possible to use the proposed methodology as an effective tool for spray targeting design for GDI engines.

Declaration of conflicting interests

The authors declare that there is no conflict of interest.

Funding

Financial support for this research was provided by Magneti Marelli Powertrain, Bologna (Italy).

References

1. Zhao F, Lai M-C and Harrington DL. Automotive spark-ignited direct-injection gasoline engines. *Prog Energ Combust* 1999; 25(5): 437–562.
2. Rivera EA, Mastro N, Zizelman J, Ooyama R and Kirwan J. Development of injector for the direct injection homogeneous market using design for six sigma. SAE paper 2010-01-0594, 2010.
3. Velji A, Yeom K, Wagner U, Spicher U, Rossach M, Suntz R, et al. Investigations of the formation and oxidation of soot inside a direct-injection spark-ignition engine using advanced laser techniques. SAE paper 2010-01-0352, 2010.
4. Zhan R, Eakle ST and Weber P. Simultaneous reduction of PM, HC, CO and NO_x emissions from a GDI engine. SAE paper 2010-01-0365, 2010.
5. Schumann F, Sarikoc F, Buri S, Kubach H and Spicher U. Potentials of spray-guided gasoline direct injection for reduction of fuel consumption and simultaneous compliance with stricter emission regulations. *Int J Engine Res* 2013; 14(1): 80–91.
6. Hemdal S, Andersson M, Dahlander P, Ochoterena R and Denbratt I. In-cylinder soot imaging and emissions of stratified combustion in a spark-ignited spray-guided direct-injection gasoline engine. *Int J Engine Res* 2011; 12: 549–563.
7. Bonandrini G, Di Gioia R, Papaleo D and Venturoli L. Numerical study on multiple injection strategies in DISI engines for particulate emission control. SAE paper 2012-01-0400, 2012.
8. Koch P, Löffler MG, Wensing M and Leipertz A. Study of the mixture formation processes inside a modern direct-injection gasoline engine. *Int J Engine Res* 2010; 11:455–471.
9. Adomeit P, Weinowski R, Ewald J, Brunn A, Kleeberg H, Tomazic D, et al. A new approach for optimization of mixture formation on gasoline DI engines. SAE paper 2010-01-0591, 2010.
10. Chen M, Zhang W, Zhang X and Ding N. In-cylinder CFD simulation of a new 2.0L turbo charged GDI engine. SAE paper 2011-01-0826, 2011.
11. Han Z, Weaver C, Wooldridge S and Alger T. Development of a new light stratified-charge DISI combustion system for a family of engines with upfront CFD coupling with thermal and optical engine experiments. SAE paper 2004-01-0545, 2004.
12. Huh KY and Gosman AD. A phenomenological model of diesel spray atomization. In: *Proceedings of the international conference on multiphase flows*, Tsukuba, Japan, 24–27 September 1991.
13. Reitz RD. Modeling atomization processes in high pressure vaporizing sprays. *Atomization Spray Technol* 1987; 3: 309–337.
14. Neumann S, Hasse C, Grasreiner S, Kleemann A, Hussmann B, Heinisch A, et al. Laser-optical and numerical study of mixture formation in a GDI engine with high tumble motion. In: *THIESEL 2012 conference on thermo- and fluid dynamic processes in diesel engines*, Valencia, Spain, 11–14 September 2012.
15. Wallesten J, Lipatnikov A and Chomiak J. Modeling of stratified combustion in a direct-ignition, spark-ignition engine accounting for complex chemistry. *P Combust Inst* 2002; 29(1): 703–709.
16. Bai C and Gosman AD. Mathematical modeling of wall films formed by spray wall interaction. SAE paper 960626, 1996.
17. ESI Group. OpenFOAM website, http://www.openfoam.org (2012).

18. Lucchini T, D'Errico G, Brusiani F, Bianchi GM, Tukovic Z and Jasak H. Multi-dimensional modeling of the air/fuel mixture formation process in a PFI engine for motorcycle applications. SAE paper 2009-24-0015, 2009.
19. Lucchini T, D'Errico G and Fiocco M. Multi-dimensional modeling of gas exchange and fuel-air mixing processes in a direct-injection, gas fueled engine. SAE paper 2011-24-0036, 2011.
20. Montanaro A, Allocca L, Ettorre D, Lucchini T, Brusiani F and Cazzoli G. Experimental characterization of high-pressure impinging sprays for CFD modeling of GDI engines. SAE paper 2011-01-0685, 2011.
21. Lucchini T, D'Errico G, Brusiani F and Bianchi G. A finite-element based mesh motion technique for internal combustion engine simulations. In: *COMODIA 2008*, Sapporo, Japan, 28–31 July 2008, MS2-3.
22. Lucchini T, D'Errico G, Jasak H and Tukovic Z. Automatic mesh motion with topological changes for engine simulation. SAE paper 2007-01-0170, 2007.
23. Hinze JO. Fundamentals of the hydrodynamic mechanism of splitting in dispersion processes. *AIChE J* 1955; 1(3): 289–295.
24. Clerides D. *Numerical simulation of spray processes in diesel engines*. PhD Thesis, Imperial College of Science, Technology and Medicine, London, 1997.
25. Kolpakov AV, Romanov KV and Titova EI. Calculation of the rebound condition for colliding drops of sharply different sizes. *Kollodn Zh* 1985; 47: 953.
26. Matsumoto S and Saito S. On the mechanism of suspension of particles in horizontal conveying: Monte Carlo simulation based on the irregular bouncing model. *J Chem Eng Jpn* 1970; 2: 83–92.
27. Ranz W and Marshall W. Evaporation from drops. *Chem Eng Prog* 1948; 48: 142–180.
28. Foucart H, Habchi C, Le Coz JF and Baritaud T. Development of a three-dimensional model of wall fuel liquid film for internal combustion engines. SAE paper 980133, 1998.
29. O'Rourke PJ and Amsden AA. A particle numerical model for wall film dynamics in port-injected engines. SAE paper 961961, 1996.
30. Hammer J, Kufferath A and Wehmeier K. Modern GDI combustion systems with focus on fuel metering technology fulfilling future emission legislation. In: *SIA conference: the spark ignition engine of the future*, Strasbourg, France, 30 November–1 December 2011.
31. Sens AM, Maass BJ, Wirths CS and Marohn DR. Effects of highly heated fuel and/or high-pressure injection on spray formation in gasoline direct-injection engines. In: *SIA conference: the spark ignition engine of the future*, Strasbourg, France, 30 November–1 December 2011.
32. Lee J, Goto S, Tsurushima T, Miyamoto T and Wakisaka T. Effects of injection conditions on mixture formation process in a premixed compression ignition engine. SAE paper 2000-01-1831, 2000.